Resolving minute temporal seismic velocity changes induced by earthquake damage: the more stations, the merrier?

Luc Illien [1,2] Christoph Sens-Schönfelder [1] and Kuan-Yu Ke[1,3]

[1] *Helmholtz Center, GFZ German Research Centre for Geosciences,* 14473 *Potsdam, Germany. E-mail:* lillien@gfz-potsdam.de
[2] *Department of Geosciences, Potsdam Universität,* 14469 *Potsdam, Germany*
[3] *Insitut für geologische Wissenschaften, Freie Universität Berlin,* 14195 *Berlin, Germany*

SUMMARY

Ground shaking induced by earthquakes often introduces transient changes in seismic velocity monitored with ambient noise. These changes are usually attributed to relaxation behaviour following the coseismic damage in the subsurface and are of relevance for post-seismic hazard mitigation. However, the velocity evolution associated with this phenomenon can occur at very small timescales and amplitudes that are not resolved with seismic interferometry and are therefore challenging to link to laboratory experiments. A way to improve the temporal resolution of the velocity time-series is to test whether the estimation of the relative seismic velocity changes dv/v obeys the ergodic hypothesis in which the joint use of colocated stations would lead to better resolved measurements. In this study, we present results from a dense seismic array that was deployed for 2 weeks at the remarkable Patache site in Chile. Thanks to high temporal averaging capabilities, we are able to resolve seismic velocity changes in the 3–6 Hz frequency band at a 10-min resolution around the occurrence of a moderate earthquake (PGV ∼1 cm s^{-1}). We report a velocity drop of ∼0.4 per cent in the first 10 min after ground shaking. Half of this initial drop was recovered within the 2 following days. The shape of the recovery follows a log-linear shape over the whole observed recovery phase, analogous to slow dynamics experiments. When normalized by the total amount of processed data, we show that the ergodic hypothesis almost perfectly holds in our network: the dv/v signal-to-noise ratio (SNR) obtained when averaging a few observation with large stacking durations for the correlation functions is almost equal to the SNR when using a large number of observations with small stacking durations. To understand if the ergodicity is linked to a particular site property, we use the array capabilities to identify the surf at the shoreline as the source of the noise and to derive a 1-D shear velocity profile with the focal spot imaging technique and a transdimensional Bayesian inversion framework. The inversion shows that hard rocks lie close to the surface indicating that this material hosts the observed shallow velocity changes. We discuss our high-resolution measurements and attribute them to a stable noise source excited by the shore, the ergodicity property and an ideal subsurface structure. Finally, we discuss the effect of moderate earthquakes on subsurface damage and the potential relaxation processes in hard rocks.

Key words: Creep and deformation; Elasticity and anelasticity; Geomechanics; Earthquake hazards; Seismic interferometry; Seismic noise.

1 INTRODUCTION

Monitoring of seismic velocity changes obtained from ambient noise cross-correlations is now a widely used technique among seismologists. Because the seismic velocity in rocks is sensitive to many driving processes, this tool has been used to constrain various dynamics in the subsurface such as changes in groundwater (Gassenmeier *et al.* 2015; Lecocq *et al.* 2017; Clements & Denolle 2018; Illien *et al.* 2021), soil moisture (Dietze *et al.* 2020; Oakley *et al.* 2021), permafrost thickness (Overduin *et al.* 2015; Albaric *et al.* 2021; Lindner *et al.* 2021) and volcanic activity (Sens-Schönfelder *et al.* 2014; Budi-Santoso & Lesage 2016; Donaldson *et al.* 2019). The use of seismic interferometry has also enabled the study of rock properties changes in response to *in situ* strain

induced by surface temperature (Richter *et al.* 2014; Lecocq *et al.* 2017), Earth tides (Takano *et al.* 2014; Sens-Schönfelder & Eulenfeld 2019) and more notably to dynamic strain due to ground shaking during earthquakes. Indeed, there is a plethora of seismic interferometry studies that were conducted following major earthquakes (Brenguier *et al.* 2008; Nakata & Snieder 2012; Viens *et al.* 2018; Qin *et al.* 2020). Most of this literature shows two distinct phases: a short coseismic phase in which the seismic velocity drops and a post-seismic phase in which the velocity recovers in a non-linear fashion. This latter phase is called relaxation or slow dynamics and can last for several years (Brenguier *et al.* 2008; Marc *et al.* 2021). These time-dependent changes of the seismic velocity suggests that earthquakes induce a lingering effect in subsurface rock properties. This mechanical perturbation may be at the origin of other transient surface observations, which exhibit a similar time-evolution such as transient increases of aquifer permeability (Manga *et al.* 2012; Illien *et al.* 2021) or landslide rates (Marc *et al.* 2015).

The time dependency of the elastic behaviour is linked to a non-classical type of elastic non-linearity. This behaviour has been reproduced experimentally in a wide range of materials ranging from rocks (TenCate *et al.* 2000; Brantut 2015; Shokouhi *et al.* 2017) over concrete (Bekele *et al.* 2017) to unconsolidated granular samples (Knight *et al.* 1995), which suggests that this phenomena is universal (Snieder *et al.* 2016). The transient dynamics is generally interpreted as the result of (1) a phase of 'damage' during deformation that arises from a variety of contacts (Ostrovsky *et al.* 2019; Sens-Schönfelder *et al.* 2019) which are broken at grain boundaries or at defect locations and (2) a phase of 'healing' associated with thermally activated processes that bring the metastable contacts towards a new equilibrium state—a phase also called slow dynamics or relaxation (Guyer *et al.* 1999; TenCate *et al.* 2000). In rocks and near-surface geomaterials, this contact recovery is thought to happen due to microcracks and fracture closure (Meyer *et al.* 2021) or re-arrangement of frictional shear zones (Lieou *et al.* 2017) and with a large contribution of chemical processes modulated by moisture (Brantut 2015; Bittner & Popovics 2021; Gao *et al.* 2022). Corresponding physical and phenomenological models can be developed from laboratory observations thanks to a fine control of the strain disturbance (Remillieux *et al.* 2017), a well-resolved temporal acoustic monitoring system [that can observe relaxation timescales down to fractions of a second (Shokouhi *et al.* 2017)], simplified geometries (Yoritomo & Weaver 2020) or the knowledge of the physical properties of the chosen rock samples. However, the application of models to field observations is challenging due to poorly resolved velocity measurements, superimposed influences and depth-dependent properties. Indeed, the stochastic nature of the seismic ambient noise wavefield requires temporal stacking of the noise correlations to recover the stable pseudo Green's function that is required for velocity monitoring (Xu *et al.* 2021). This reconstruction controls the final time-resolution of the obtained dv/v measurements. Moreover, constraints on the subsurface structure and velocity are rarely available. These limitations prevent us from answering fundamental questions that would bridge the gap between field observations and models, which includes *what is the impact of small/moderate shaking perturbation*, *what is the shortest relaxation timescale in the field* or *in which structures/rocks the relaxation is likely to occur in the subsurface?*

To address these questions, we performed seismic interferometry study using a dense seismic array in Patache, Chile (Fig. 1) located around the permanent station PATCX in the IPOC network. This station has produced remarkable results with observations of stable velocity changes induced by the Earth's tides (Sens-Schönfelder &
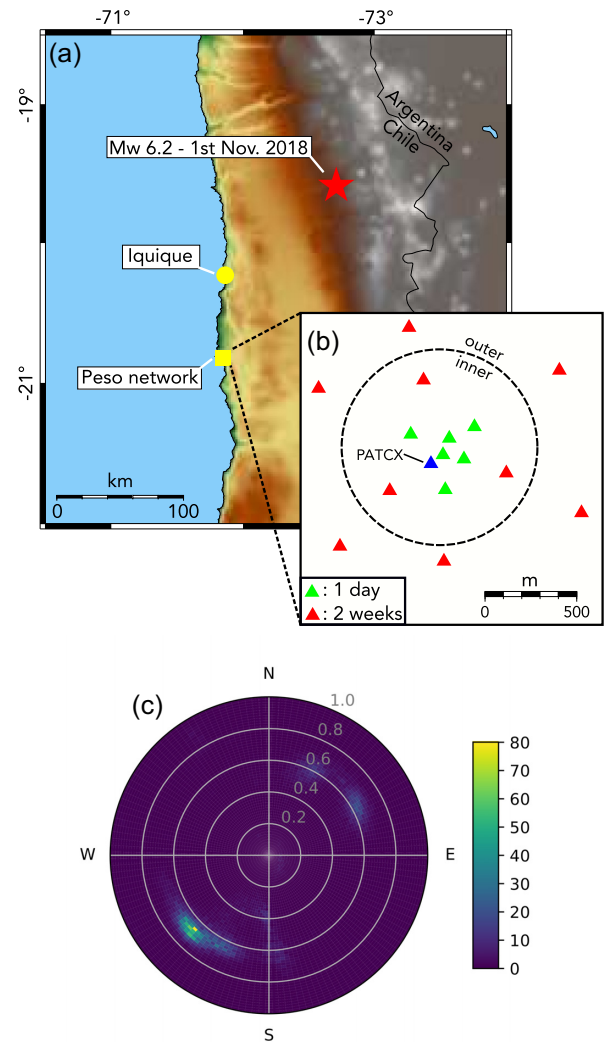

Figure 1. Map of the study area and beamforming analysis. (a) Location of the PESO array relative to Chile. The red star indicates the epicentre of the 1st of November 2018 earthquake. (b) Geometric setting of the PESO array. The blue triangle stands for the permanent PATCX station. The circle indicates our convention for the inner ring and the outer ring for this study (c) Results of the beamforming analysis. Colourbar indicates the energy level that is reported on the azimuthal plot.

Eulenfeld 2019), earthquakes (Gassenmeier *et al.* 2016) or temperature (Richter *et al.* 2014). The relative success of these studies suggests that the conditions at this site are particularly suited for monitoring studies. In this paper, we attempt to investigate these specific conditions and increase the time-resolution of the velocity changes retrieval at Patache with the ergodic hypothesis (Moore 2015). We assume that the average statistical properties of the diffuse noise wavefield across the dense network (the ensemble average) during a short time interval at time t is similar to the average statistical properties recorded at one station over a larger time span (the time average). If this assumption holds, by spatially averaging the results obtained from colocated stations, one can significantly reduce the time window needed for stacking correlation functions and therefore improve the time-resolution of stable velocity change measurement δv. This hypothesis has been made implicitly in previous studies (Sens-Schönfelder *et al.* 2014; Illien *et al.* 2022) but not tested. Here, we address the validity of this assumption explicitly.

Using this technique, we report stable observations of velocity changes at a 10-min resolution for a period of ∼2 weeks. During this interval, we measure a coseismic velocity drop of 0.4 per cent amplitude and a well-resolved subsequent recovery in the 3–6 Hz frequency band. Utilizing the dense network, we also compute the local Rayleigh wave dispersion curve using the focal spot imaging technique. We invert the obtained results for a 1-D shear velocity profile using transdimensional Bayesian inversion and show that the relaxation changes are hosted in a hard rock site. The characterization of the site also allows to highlight advantageous conditions for stable dv/v measurements.

We describe the data and methods in Section 2. In Sections 3.1 and 3.2, we present the seismic velocity changes results and the inferred 1-D shear velocity profile obtained at our field site. Section 4 is dedicated to the discussion, notably on the stability of the velocity estimates and the relaxation processes in hard rocks. Conclusions are in Section 5.

2 DATA AND METHODS

2.1 The Peso array

The Peso array consists of 15 geophones (3-components) located around the broad-band station PATCX of the Chilean IPOC network (GFZ Potsdam & CNRS-INSU 2006, Fig. 1). Stations were installed on the 21st of October 2018 with nine stations recording for ∼2 weeks while the others were relocated after ∼1.5 d. The array geometry was designed in a circular-triangular pattern to maximize different interstation distances and optimize the usability for different tasks such as the study of the noise sources, the investigation of the subsurface velocity structure and the monitoring of velocity changes. Placed on top of an escarpment located at 70 km south of Iquique city (Figs 1 and S1), the stations have an elevation of about 600 m above sea level. After performing a beamforming analysis (method in Text S1), we estimate that the array is strongly dominated by waves propagating in the network from the southwest direction with a slowness of 0.65 s km^{-1} (Fig 1c).

2.2 Seismic interferometry for retrieving relative seismic velocity changes

We compute ambient noise cross-correlations to estimate relative seismic velocity changes dv/v (Sens-Schönfelder & Brenguier 2019) using the stations that were installed for 2 weeks (nine stations) and the permanent station PATCX (Fig. 1). We first pre-process the seismic traces to limit the effect of high-amplitudes arrivals such as earthquakes on the correlations. These signals are numerous in the seismically active continental margin of northern Chile due to many small earthquakes (Gassenmeier *et al.* 2016; Sens-Schönfelder & Eulenfeld 2019). To minimize unphysical bias introduced by non-linear normalization schemes such as the 1-bit normalization or spectral whitening (Fichtner *et al.* 2017), we choose a statistical approach to identify the time segments which contain the short-term high amplitudes and remove them from the analysis.

Due to its multiple scattering nature, the recorded seismic wavefield follows a Gaussian probability distribution (Groos & Ritter 2009). The amplitudes of the envelope of such a field are Rayleigh-distributed. The corresponding distribution is defined by a single scale parameter β (McNicol 1949; Oshima & Takenaka 2020):

$$p(a) = \frac{a}{\beta^2} \exp\left(\frac{a^2}{2\beta^2}\right), \tag{1}$$

where $p(a)$ denotes the probability density of the envelope amplitudes a.

The ballistic arrivals and coda waves induced by a seismic event or a local disturbance unavoidably superpose on the background noise and increase the amplitude of the recorded field, changing the scale parameter β. Our approach consists of building amplitude predictions based on an estimate of β dominated by the background noise and compare it to short-term estimates of the mean squared envelope that are dominated by large transient amplitudes.

In a first step, we filter the seismograms and compute the envelopes $a(t)$ using the Hilbert transform. The mean of the logarithm of the envelope is linked to the scale parameter β through the log-Rayleigh distribution (Rivet *et al.* 2007). Since the mean of the logarithm down-weights large amplitude samples, we obtain an estimate of β that characterizes the amplitude of the background field. According to Rivet *et al.* (2007), β can be retrieved from the following relationship:

$$\beta_1 = \exp\left[\overline{\ln a(t)} - \frac{1}{2}(\ln 2 - \gamma)\right]. \tag{2}$$

In this equation, γ is the Euler's constant and $\overline{\ln a(t)} = 1/N \sum_i \ln(a_i)$ is the logarithm of the geometric mean. Corresponding computations were performed in 1-hr segments to down-weight furthermore the short-lived high amplitudes of earthquakes or other local disturbances. The assumption is that these disturbances, despite potentially being orders of magnitudes larger than the background, do not significantly bias this estimate of β due to the logarithm and the long term averaging. β_1 can be used as a prediction of background amplitude even if perturbations superpose the recorded signal.

In a second step, we obtain a short term estimate over 1-min time windows of β with the intention to identify the high amplitude disturbances. Therefore, we estimate β from the mean squared envelope (McNicol 1949):

$$\beta_2 = \sqrt{2} \, \overline{a^2} \tag{3}$$

with $\overline{a^2} = 1/N \sum_i a_i^2$ being the arithmetic average of the squared envelope. If the seismic signal is Rayleigh-distributed with a stationary scale parameter, the two estimates β_1 and β_2 will be equal. Short disturbances superposing the background signal are very well discriminated by the ratio β_2/β_1 even for fairly small additional signals.

We illustrate this process in Fig. 2 by comparing the amplitude of the signal, the predicted background signal amplitude derived from β_1 and the short-term high amplitude estimate derived from β_2. To identify segments containing disturbances, we calculate the ratio of β_2/β_1 and compare it to a threshold value I that we set equal to 1.6 based on visual inspection of the performance. We construct a mask that we set to zero for all 1-min segments with $\beta_2/\beta_1 > I$ and to 1 otherwise (Fig. 2b). In a last step, we taper the edges of the mask and save it to a file. We build masks for every station of the network using the vertical component filtered in a narrow band centred at 4 Hz. On average, we found that 10–40 per cent of the seismic traces were muted depending on the day and the station considered (Fig. S2).

Following the previous calculations, we trim the traces to 1-min segments and resample the data at 50 Hz. We taper and filter the data in the 3–6 Hz frequency band. This band was chosen because of the stable results it has provided in previous studies at this site (Richter *et al.* 2014; Gassenmeier *et al.* 2016; Sens-Schönfelder & Eulenfeld 2019). Finally, we mute the raw traces with the computed
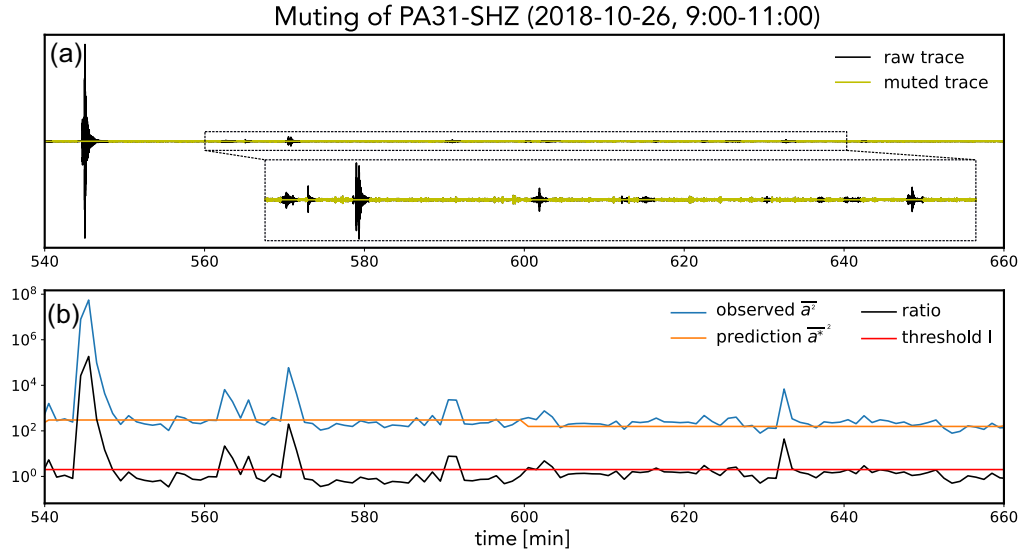
Figure 2. Muting of the seismic trace, an example. (a) The black trace shows 2 hr of vertical data at the station PA31. The other trace stands for the muted version with a close-up for clarity. (b) The blue line indicates the estimates of β_2 based on the average squared envelope of the raw trace shown in (a) at a 1-min resolution. Orange line shows the prediction of β_1 based on the squared envelope predicted by the log-Rayleigh distribution at each hour. The ratio of the observation and the prediction is shown in black with the red line indicating the threshold used for muting the raw trace.

masks (Fig. 2). We calculate all possible cross-correlation combinations which include all autocorrelations AC (ZZ, EE, NN, 30 combinations), single station cross-correlations SC (ZN, ZE, EN, 30 combinations) and interstation cross-correlations CC (nine components cross-correlation tensor after rotation for 405 combinations). We cross-correlate the 1-min segments and stack the results over intervals of 10 min.

To estimate the average relative velocity changes dv/v, we use the *stretching* technique (Sens-Schönfelder & Wegler 2006), assuming the velocity changes are spatially homogeneous. For each combination, we compute the stretched versions of the correlation functions $C(t_i, \tau)$ where t_i is the date and τ is the lapse time of the correlation function. We use the 7–16 s lapse time window ($[\tau_1, \tau_2]$) and compare them to a unique reference ξ_r that is taken as the average cross-correlation function of the whole time period. This allow us to form the similarity matrix with ε_j being the stretching factor:

$$R_r(t_i, \varepsilon_j) = \int_{\tau_1}^{\tau_2} C(t_i, \tau)\xi_r(\tau * (1 + \varepsilon_j))\mathrm{d}\tau. \tag{4}$$

These similarity matrices $R_r(t_i, \varepsilon_j)$ can be all stacked to obtain the final dv/v representative for the entire field site (Fig. S3). Details for calculations can be found in Illien *et al.* (2021) in which we used the same computation scheme for the velocity changes estimation.

2.3 Estimation of the Rayleigh wave dispersion curve

To constrain the range of absolute velocities in which the relative changes dv/v occur and resolve the subsurface structure at our field site, we estimate the average 1-D Rayleigh wave dispersion curve. We use the data recorded on the 22nd of October by the 16 stations network (Fig. 1) to maximize the number of available interstation distances. We pre-process the traces by correcting for the instrument responses, filtering in the 0.25–16 Hz range and muting high-amplitudes arrivals with the technique described in Section 2.2.

We use the focal spot imaging technique to obtain Rayleigh wave phase velocities (Hillers *et al.* 2016). This technique is based on

the spatial width of the zero lag cross-correlation field and aims to reconstruct the high-amplitude focal spot that emerges due to time-reversal properties (Conti *et al.* 2002; Fink 2008). To normalize amplitudes between the different stations, we compute in the Fourier domain the cross-coherence γ. For two stations A and B, we have

$$\gamma_{AB}(w) = \frac{u_A(w)u_B^*(w)}{|u_A(w)||u_B(w)|} \tag{5}$$

with u_A and u_B being the waveforms recorded at stations A and B and w the angular frequency. We perform the computation on hourly segments and stack the 24 resulting cross-coherence functions of the 22nd of October for each ZZ interstation combination. We assume that the wavefield is dominated by Rayleigh waves. In this case, the cross-coherence amplitudes at the zero lag time τ (for ZZ combinations) can be expressed as (Hillers *et al.* 2016)

$$A(r, \tau = 0) \sim \sigma J_0(kr)e^{-\alpha r}. \tag{6}$$

In this equation, r is the interstation distance, k is the wavenumber, σ is a scaling constant that accounts for the pre-processing and α is an apparent attenuation coefficient. J_0 is the Bessel function of the first kind. The first zero crossing of eq. (6), which determines the size of the focal spot, is located at

$$r^0 = \frac{3}{8}\lambda \tag{7}$$

and therefore completely determines the wavelength λ. From fitting relation eq. (6), one can see that phase velocities for different frequencies can be obtained with a suitable interstation distance coverage r. To obtain w, we apply a 0.5 Hz wide bandpass filter on the cross-coherence functions centred around target frequencies between 0.5 and 2.75 Hz with a frequency increment of 0.25 Hz. We fit the data in a procedure similar to Hillers *et al.* (2016): we first use all the available amplitudes to obtain a first estimate for the wavelength λ (red lines in Fig. 3). Then, we fit the combinations that are within the first 0.7 λ (green lines in Fig. 3) to obtain a second improved estimate. At distances larger than one wavelength, the estimation can be contaminated by scattering and topography effects (Hillers *et al.* 2016), hence we estimate the velocity closer to
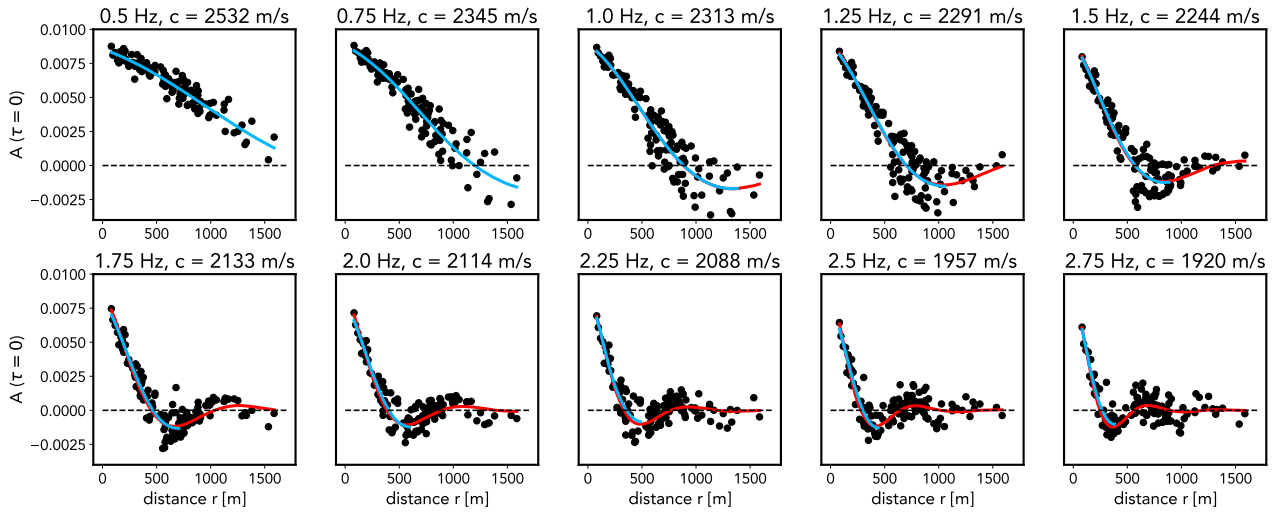
Figure 3. Focal spot fitting results. Each plot indicates the result from a different central frequency (indicated in the titles with the corresponding inferred phase velocity). *Y*-axis represents the amplitude of the cross-coherence ZZ functions at zero lag time while the *x*-axis shows the interstation distance. Red and blue lines show the fitting from the first iteration and second iteration respectively. Dashed lines indicate the 0 amplitude.

Table 1. Parameters priors used in the inversions.

Vs [km s^{-1}]	(0.5, 4)
z [km]	(0, 1)
Number layers	(1, 12)
Vp/Vs	(1.5, 2.2)
Noise [km s^{-1}]	(1e-4, 1e-1)

the first 0 crossing. We obtain 10 measures for the dispersion curve that we re-interpolate to 20 data points with the Geopsy software.

2.4 Inversion of the 1-D shear velocity profile

We invert the dispersion curve with BayHunter (Dreiling & Tilmann 2019; Dreiling *et al.* 2020), a python package dedicated to Markov chain Monte Carlo transdimensional Bayesian inversion. The main advantage of a Bayesian inversion is the retrieval of an ensemble of models and a better assessment of uncertainties in the retrieved solutions. Another advantage is that the model complexity, that is the number of layers (hence *transdimensional*) and the noise in the data are unknown hyperparameters that are determined during the inversion process. For more details regarding the algorithm, we refer the reader to the paper of Bodin *et al.* (2012) and the documentation of BayHunter (Dreiling & Tilmann 2019).

In this paper, we focus on estimating a shear-velocity profile and the V_P/V_S ratio. We give a range of possible solutions for these physical parameters and the hyperparameters as priors for the inversion (Table 1). 50 Monte Carlo chains are initialized to explore enough possibilities in the parameter space, using a total of 772 608 iterations with a 2:1 ratio between the burn-in phase (initial exploration) and the exploration phase in which we look for the possible models. Some of the chains fail to converge as they return significantly smaller likelihoods than most chains after the burn-in phase: The threshold controlling the convergence is a percentage (here taken as 95 per cent) of the maximum reached median likelihood from the chain ensemble. The chains not reaching this median likelihood are declared outlier chains. The final posterior distribution gathers 100 000 models by subsampling all non-outlier chains. We interpolate the results at a 50 m resolution.

3 RESULTS

3.1 Relative seismic velocity changes

3.1.1 The dv/v time-series

Measurements of relative seismic velocity changes for each individual cross-correlation combination appear to be strongly scattered, although the measurements converge towards a clear dynamics when all plotted together (black dots, Fig. 4a). To illustrate the precision that can be obtained with a single station we show the measurements jointly obtained using the six possible combinations of the permanent station PATCX (autocorrelations and single-station cross-correlations) with the blue curve in Fig. 4(a). The highest precision is obtained when using all combinations in the network, reducing the noise to an apparent ∼0.05 per cent (red line, Fig. 4). For all measurements, we observe periods with larger scatter that we attribute to changes in the noise wavefield (Fig. S4). These changes are seen in the traces amplitudes computed when building the pre-processing masks (Fig. 4b). We attribute the larger amplitudes (obtained here at 4 Hz) to strong winds in the afternoon.

We observe little to no velocity changes from the 22nd of October to the 1st of November. A clear drop of ∼0.4 per cent is then visible and simultaneous with the M_w 6.2 earthquake that occurred at ∼150 km from the array (Fig. 1a). Averaging all horizontal component envelopes in our network, we measure a ground shaking intensity of the event to ∼1 cm s^{-1} PGV (Fig. S5). Half of the initial velocity drop was recovered after 2 d, with strongest recovery at early times after the coseismic drop. The duration of our data is not sufficient to see a full recovery, hence reduced velocities appeared sustained for the observation time.

3.1.2 Stability of the measurement

We quantify the effect of multiple station averaging relative to the noise level in the final dv/v estimation. The standard deviation of the velocity time-series dv/v over all time samples of the 10 d prior to the earthquake can be plotted as a function of the stacking duration window and the number of combinations used (Fig. 5). Assuming
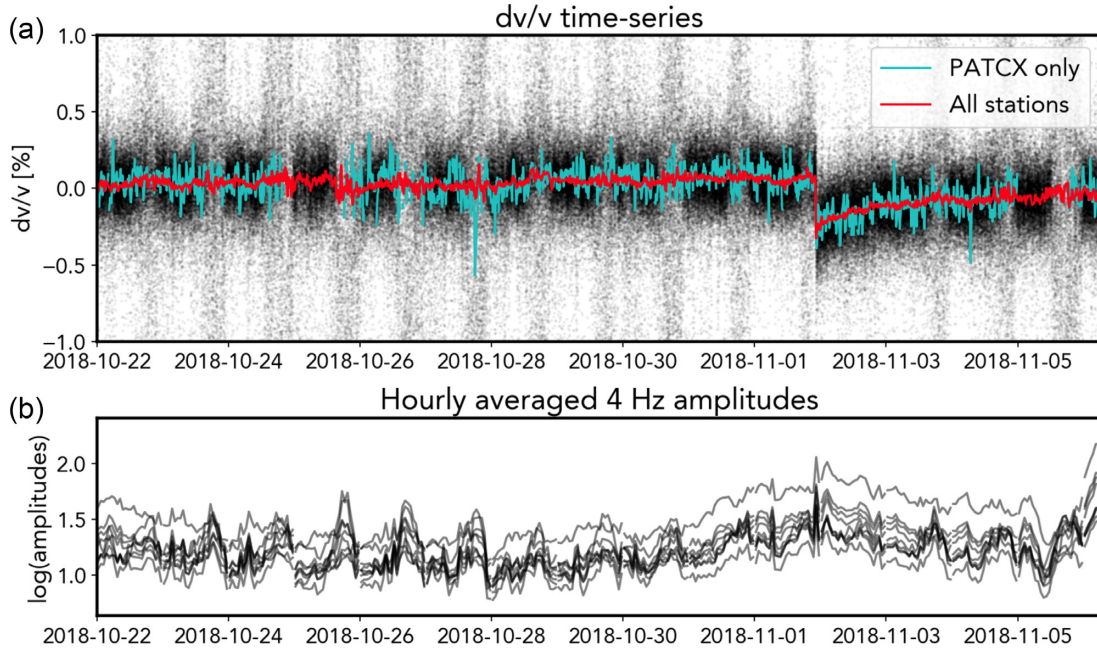
Figure 4. PESO dv/v time-series. (a) Each black dot indicates an estimation using a single cross-correlation combination in the network. Blue line shows the joint result using the six self-combination of the PATCX station. Red line shows the results using all 405 combinations. Time resolution is 10 min. (b) Noise amplitudes time-series at 4 Hz. Each lines represents the hourly logarithm of the hourly averaged noise amplitudes for all the stations deployed during the 2 weeks. Opacity is a function of the curves overlap. Traces were processed with a 4 Hz Gaussian filter beforehand.
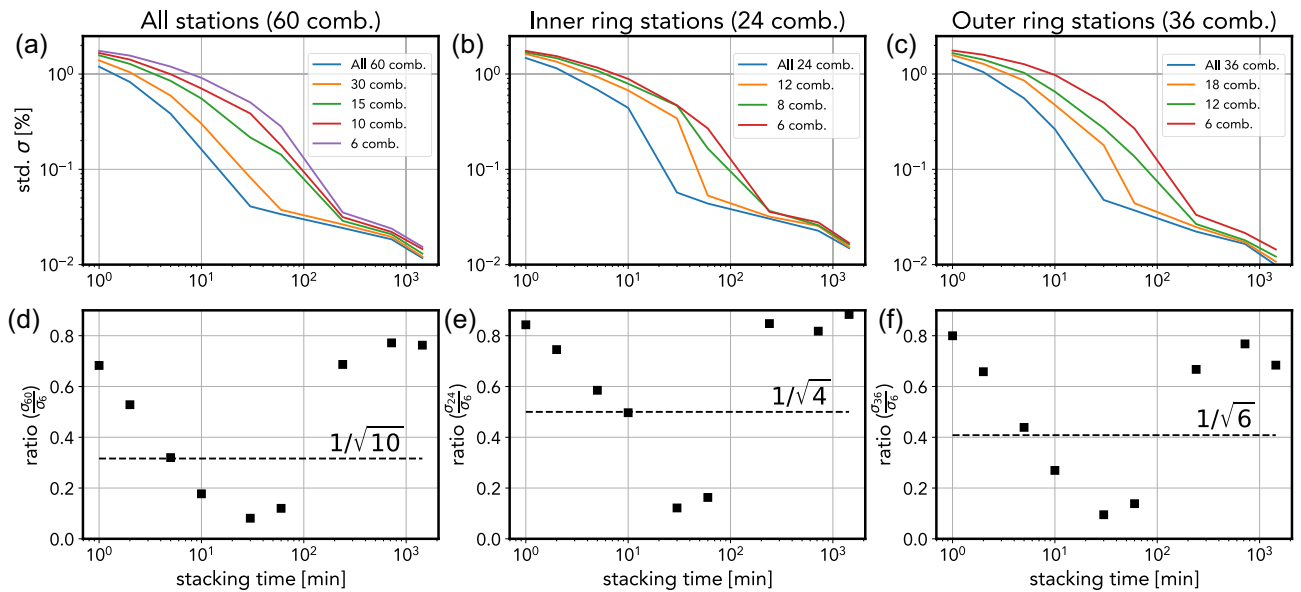

Figure 5. Standard deviations of the dv/v changes prior to the earthquake (from the 22nd of October to the 1st of November) obtained using different stacking durations and number of combinations (a) Curves obtained using all single-combinations in the network. For each stacking duration, the mean of the standard deviation of the respective combination subset. The subsets are characterized by a number of combination shown as an inset label. We show on (b) and (c) the same plot but using only the inner ring stations and the outer ring stations respectively. The subplots (d), (e) and (f) show the corresponding ratio between the standard deviation using all considered combinations and when using only six. The dashed line shows the theoretical reduction of the standard deviation for independent variables with the same mean and variance.

that the velocity variations during this time-span is mostly due to noise, this standard deviation is a good proxy of the signal-to-noise ratio of (SNR) of the dv/v time-series and for the measurement stability. Because we exploit a late time-window (starting at 7 s, which corresponds to ~21 wavelengths at 3 Hz, the lower limit of the used bandpass) in the correlation function for measuring the dv/v changes, we ensure to minimize diurnal physical changes

that arise when processing earlier times (Richter *et al.* 2014; Sens-Schönfelder & Eulenfeld 2019). To construct the plot, we use all six self-correlations (AC+SC) for each of the 10 stations. We restrict the analysis to self-correlations for purely economical reasons here, since interstation observations would yield similar results at this combination of distance, wavelength and lapse time. After shuffling the 60 combinations randomly in a list, we split them into
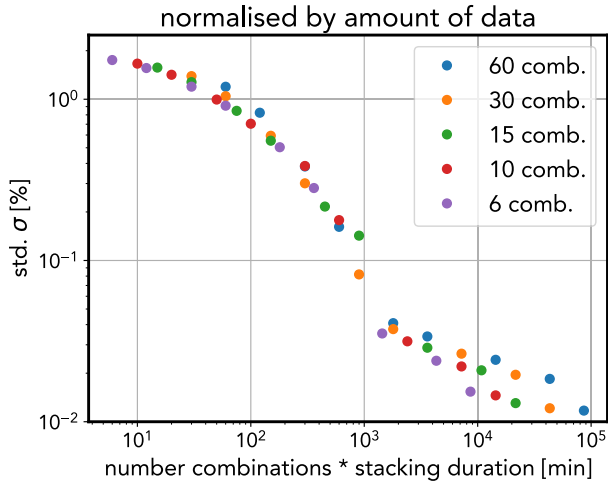
Figure 6. Noise in the seismic velocity time-series normalized by the total amount of used seismic data. Data are identical to Fig. 5(a) but normalized by the total added length of the used seismic traces.

multiple subsets corresponding to 6 (10 subsets), 10 (6 subsets), 15 (4 subsets) and 30 combinations (2 subsets). For each subset, we average the velocity changes using the similarity matrix stacking (eq. 4) described in the methods (Section 2.2) and extract the standard deviation of the obtained dv/v. We perform these calculations at several time resolution using different durations for the stacking window of the correlation functions ranging from 1 min (no stacking) to 1 d stack. Finally, we also build the plots considering only the inner-ring stations (interstation distances from 260 to 670 m) and the outer-ring stations (interstation distances from 570 to 1580 m). The ring conventions are shown in Fig. 1(b).

The standard deviation always increases when using a lower number of combinations (Figs 5a–c). For all curves, smaller stacking duration consistently also yields larger standard deviations. However, this deterioration systematically happens at different thresholds depending on the number of combinations used (Figs 5a–c). This threshold is important as it drives the transition towards standard deviations that can be one order of magnitude higher at smaller time-resolution. Surprisingly, for large time windows, the average standard deviation of the outer ring stations (36 combinations, Fig. 5c) is smaller than the average using all combinations (Fig. 5a).

To illustrate the improvement of the estimations when using more stations, we plot the ratios between the standard deviations measured with many combinations (60, 24 and 36 combinations depending on the configuration) and the one measured with six combinations, which is the amount of information that would be obtained with one station (Figs 5d–f). Theoretically, the reduction of the standard deviation of a sum of independent random variables with the same mean and variance should obey to a factor of $1/\sqrt{N}$ with N being the number of variables. For all combinations, we indicate this theoretical reduction using $N = 10$ (10 stations), $N = 4$ for the four inner ring stations and $N = 6$ for the six outer ring stations. We observe that the improvement of the dv/v result is not significant at both large time-windows and at small-time windows (Figs d–f) for the three considered configurations. However, in an intermediate sweet spot, the ratios reach the theoretical reduction limit and even plot at lower values.

Finally, we normalized the standard deviations shown in Fig. 5(a) by the amount of data used to obtain a velocity estimation. The resulting plot shows a remarkable collapse of the data point along a single non-linear decreasing trend (Fig. 6). Using our averaging

method, the same SNR can be achieved by either using more stations and smaller stacking time-windows or using less stations with more stacking, as long as the same amount of 'information' is used. Under these conditions, the ergodicity property can therefore be validated. Practically, this also means that a good precision can be obtained with one station at the cost of having larger stacking time and therefore a lower time-resolution. We note that above the 10^3-min mark, the standard deviations exhibit a step change and the agreement between the points is less striking. Knowing that small daily velocity changes due to temperature (Richter *et al.* 2014) or the Earth's tides (Sens-Schönfelder & Eulenfeld 2019) are active at the Patache field site, we attribute the degradation to physical effects that are more or less smoothed or averaged at large stacking times depending on the number of used combinations.

3.2 Shear velocity profile

The inverted 1-D shear velocity profile is shown in Fig. 7(a) along with the target dispersion curve which we inferred from the focal spot imaging technique (Fig. 7c). The average shear velocities are in the 1250–2000 m s^{-1} range (mean = 1600) in the first ∼200 m and in the 2400–3200 m s^{-1} range (mean = 2750 m s^{-1}) in the ∼ m depth range. The profile and the histogram of the layers depths is characterized by a clear two-layer structure (Figs 7a, b and d) with absolute seismic velocities indicating a hard-rock site. Most of inferred models result in smoother version of the target dispersion curve (Fig. 7c) with a noise level in the measurements estimated at a 25 m s^{-1} median value (Fig. 7e). The V_p/V_s ratio is poorly constrained but exhibits a median value of 1.58, typical of crystalline rocks or consolidated sediments (Mavko *et al.* 2009).

We note that the average velocity value inferred in the shallow surface (∼1600 m s^{-1}) shows a rather good agreement with the apparent velocity (∼1500–1600 m s^{-1} in the 4–6 Hz frequency range) inferred from the beamforming analysis performed to characterize the noise distribution (Fig. 1c). To refine the velocity profile, we performed a second inversion with the same method, adding the rough estimate of the high frequency phase velocity obtained from the beamforming analysis (velocity at 1550 m s^{-1} at ∼4 Hz) to the target dispersion curve (Fig. S6). The obtained velocity profile emphasizes the 2-layer structure with a discontinuity at ∼200 m depth and refines the shear velocity to 1550–1600 m s^{-1} in the superficial layer and ∼2750 m s^{-1} in the second layer. However, these secondary results should be interpreted with caution, as velocity measurement with beamforming may be flawed due to the potential steep incidence of body waves (Rost & Thomas 2002).

4 DISCUSSION

4.1 Conditions for stable velocity measurements

Finer time-resolution using passive seismic monitoring is a long standing challenge in seismic interferometry. Previous attempts to tackle this issue include denoising the cross-correlations with adaptive filters (Hadziioannou *et al.* 2011) or convolutional autoencoders (Viens & Van Houtte 2020), performing single-station cross-correlation at higher frequencies (Hobiger *et al.* 2014), stacking more short time-windows instead of a lower number of long time-windows (Xu *et al.* 2021) or tracking a persistent phase in the correlation functions (Lu & Ben-Zion 2022). In our study, we took the simple road of combining more stations for testing the ergodicity of the seismic velocity estimated from the noise wavefield.
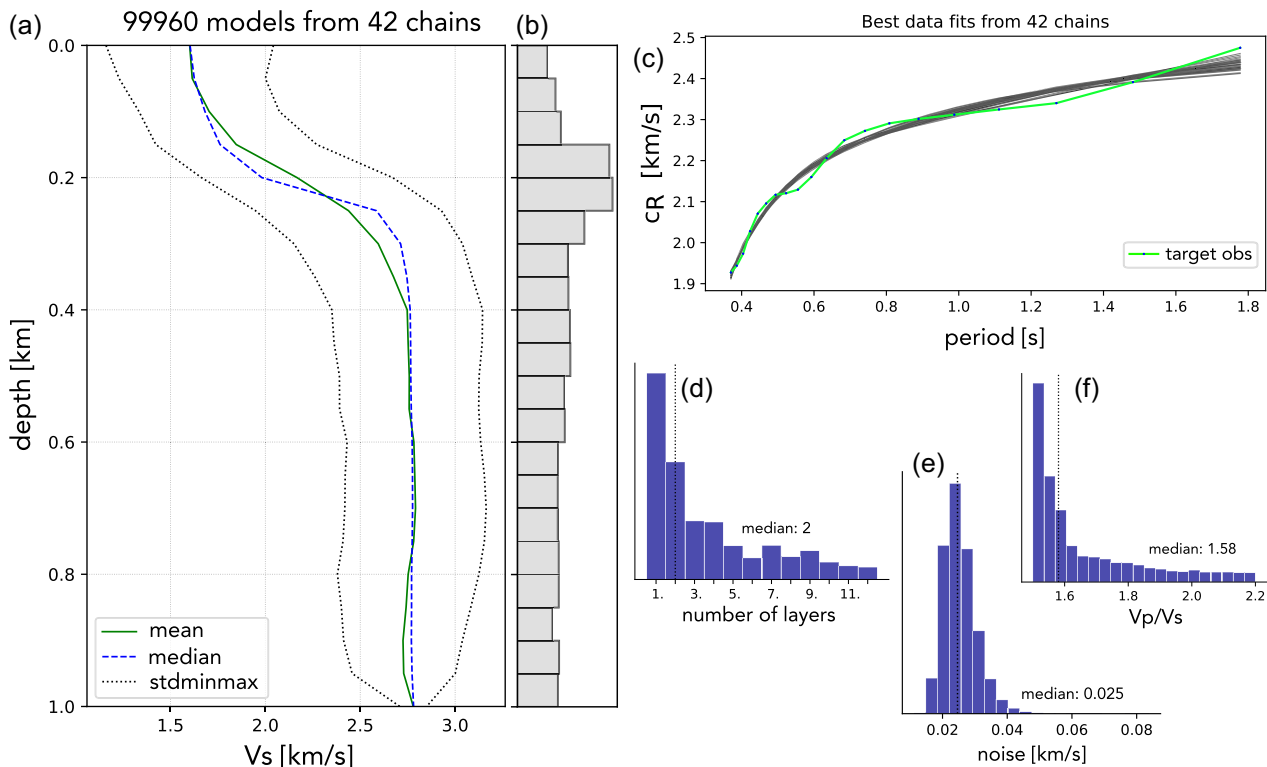
Figure 7. Inversion of the 1-D shear velocity profile and corresponding target dispersion curve. (a) Inferred shear velocity profile interpolated at a 50 m resolution. Green and blue lines shows the mean and the median value of the best retained models. Dashed black lines indicate the standard deviation. (b) Histogram of the depth of the inferred layer structures (c) The green line shows the dispersion curve that we use for the inversion, the other curves showing the best fit obtained for each chains. Histograms corresponding to the other inverted parameters are shown in (d) for the number of layers, in (e) for the noise level in the measurements and in (f) for the *Vp/Vs* ratio.

The velocity change measurements were improved, with a noise level down to one order of magnitude lower than the one obtained with one station (six combinations), depending on the length of the stacking window (Fig. 5). The theoretical limits plotted in Figs 5(d)–(f) give a limited prediction of this improvement which indicates that our assumption of independent variables with the same mean and variance may not hold. However, at intermediate stacking length, the refinement of the results is clear (Figs 5d–f). Outside of this intermediate range, the benefits are limited: With small stacking windows, the space-averaging is not sufficient to counter-balance the requirement of a minimum time duration for an effective statistical noise source summation (Fichtner *et al.* 2017). At the other end, with large stacking windows, the time-averaging is long enough for stable measurements and is not improved greatly when adding more stations. We conclude that the sweet spot between these conditions could be constrained with pilot deployments to optimize the number of stations needed for high-resolved temporal measurements. The plot of the dv/v recovery phase at different time resolutions highlights the trade-off between the choice of a time-resolution and the addition of noise in the time-series (Fig. 8). Ultimately, the ergodicity hypothesis was satisfied as long as the same amount of data was used (Fig. 6), suggesting that the stacking time of the correlation functions should be decided upon the number of available stations.

We found no significant effects when using different interstation distances (Figs 5b and c). However, the effects of this parameter should be investigated further because it is thought to be critical for optimized measurements as it controls the overall correlation of the observed wavefield at the different stations (relative to the targeted
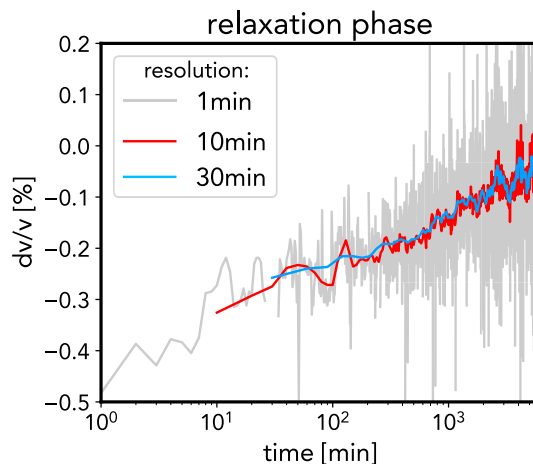

Figure 8. Relaxation phase recorded by the PESO array at different resolutions. The recovery phase shown in Fig. 4 using all the combinations is plotted in red. The log-linear *x*-axis emphasizes the characteristic slow dynamics recovery. Note the variation of noise at high-resolution (dt = 1 min) and at lower resolution (dt = 30 min).

monitoring frequency). The largest correlation should be obtained when the interstation distance is on the order of the monitoring wavelength λ. At 3–6 Hz and using 1600 m s^{-1} for Rayleigh waves, we obtain $\lambda \sim 266-533$ m. With the 90–1600 m range in our array, we have therefore a mixture of correlated and uncorrelated arrivals. At large distances, the observed dv/v changes are also caused by

different structural changes and the spatial averaging is not useful anymore.

Beyond methodological aspects, the monitoring of seismic velocity requires certain noise and structural conditions for stable measurements. Regarding noise source distribution, the reconstruction of the Green's function from correlations requires random and isotropic noise sources (Lobkis & Weaver 2001), a condition that is unlikely met in the field (Mulargia & Castellaro 2013). Nevertheless, a stable localized noise source is sufficient for monitoring purposes (Hadziioannou *et al.* 2009) and represents another ideal situation. In our frequency band, the beamforming analysis shows that the incoming energy has one dominant azimuthal direction (Fig. 1c). This feature suggests that the Peso field site is continuously excited by the same source which is likely to be induced by the surf of the ocean waves hitting the shoreline (Fig. S1). This stable situation is disturbed during windy afternoons, which cause the degradation of our velocity measurements (Fig. 4) due to high-amplitude arrivals. In our study, a statistical pre-processing scheme was designed to limit the disturbances from these deterministic signals. The 1-D profile also suggests that a low velocity layer is present at the surface (Figs 7a and b) with elevated velocities (>1000 km s^{-1} for most of inferred models, Fig. 7a). Considering a low-velocity layer of $V_S = 1600$ m s^{-1} with a thickness $H = 200$ m, we can estimate an approximate resonance frequency with $f_k = ((2k + 1)/4)/(V_S/H)$ (Nakamura 2000). With this relation, we obtain $f_0 \sim 2$ Hz to for the fundamental mode and $f_1 \sim 6$ Hz for the first overtone, these values being almost in the range of the 3–6 Hz band we used in this study. This configuration could promote the trapping and reverberation of seismic energy around this specific frequency band and with limited dissipation which are ideal conditions for monitoring subsurface changes (Sheng *et al.* 2021).

4.2 Relaxation in the field: timescales and geological structures

Following the 1st of November 2018 earthquake, we report a 0.4 per cent velocity reduction in the first 10 min after the earthquake. The observable slow dynamics behaviour lasted roughly for ∼2 d and is well resolved at the 10-min resolution (Fig. 4) with a characteristic log-linear recovery (Fig. 8). A minimum timescale of relaxation was not observed (Snieder *et al.* 2016; Shokouhi *et al.* 2017) and if it exists, must be below our 10-min resolution. The dv/v time-series obtained at 1-min resolution resolves an additional 0.1 per cent drop at earlier relaxation times, albeit an increase in noise measurements according to previous analyses (grey line in Fig. 8). Such minute seismic-induced velocity changes in both amplitude (less than 0.5 per cent) and timescale were not observed at this relatively high frequency band (3–6 Hz) to our knowledge. We used a late time window to ensure minimizing source artefacts and sampling a large portion of the subsurface. Rapid velocity changes were also reported in the literature but often using different techniques that may be more prone to noise source changes and near-surface non-linearity: Using very early times in autocorrelation functions during earthquake ground motion at frequencies above 10 Hz, the technique lead to comparatively larger changes (>5 per cent) for very small PGV ($<10^{-4}$ m s^{-1}; Bonilla *et al.* 2019). Another remarkable time-series (at a 10-min resolution) was obtained using *P/S* converted waves following the M_w 7.1 Ridgecrest earthquake (Lu & Ben-Zion 2022). However, their observed changes are larger than our results due to significant ground shaking. Our study suggests that small ground shaking induces a lingering

effect that may be challenging to resolve. These effects matter for understanding the effect of cumulative aftershocks for the recovery of material properties after large earthquakes (Sawazaki *et al.* 2018). Our temporal coverage was not sufficient to estimate the maximum relaxation timescale of the recovery. In a previous study we hypothesized that material properties and ambient conditions are the dominant control of the observable maximum relaxation time, rather than the coseismic ground shaking intensity (Illien *et al.* 2022). A dynamic system analysis on a longer time-series could help us shed light on these controls and assumptions and is planned in a future manuscript.

In field studies, relaxation mechanisms are often interpreted as near-surface non-linearity induced by soils deformation (Sleep & Nakata 2017; Viens *et al.* 2018; Guéguen *et al.* 2019). Pictures from the field (Fig. S7) indicate the presence of a conglomerate with evaporites at the surface, which may constitute the first 200 m layer (Fig. 7a). If we assume the dominance of Rayleigh wave energy in the noise wavefield, the corresponding sensitivity kernel [computed with the scheme of Herrmann & Ammon (2002)] associated with the measured dispersion curve (Fig. 7c) and the inferred 1-D model (Fig. 7a) suggest that these rocks host the observed velocity changes at frequencies above 3 Hz (Fig. S8). The higher velocity in the second layer could correspond to crystalline rocks such as Gabbros, according to geological studies in the area (Tapia *et al.* 2018). In the laboratory, relaxation has been observed in crystalline (Shokouhi *et al.* 2020; Meyer *et al.* 2021) and sedimentary rocks (Brantut 2015). Numerical simulations and experiments suggests that the largest contact areas in the rock fractures (Shokouhi *et al.* 2020), cracks (Gao *et al.* 2019) and the grain contacts in granular media (Kober *et al.* 2022) controls the relaxation timescale. Due to higher strength, hard rocks can sustain larger flaws and fractures, which in turn may lead to longer relaxation timescale due to high activation barriers. This statement may only be valid if slow dynamics behaviour effectively originates due to thermally activated processes such as with the Arrhenius equation (Snieder *et al.* 2016; Ostrovsky *et al.* 2019).

5 CONCLUSIONS

In this study, we explored the potential advantage of using more colocated stations to improve the time resolution of relative seismic velocity changes dv/v inferred from ambient noise correlations. We made the assumption that the dv/v estimation obeys the ergodic hypothesis, that is the time-average (one station with large stacking time for the correlation functions) is equal to the space-average (several stations with small stacking time for correlation functions). We found that the staking time required to obtain stable correlation functions and therefore velocity measurements can be significantly lowered by using more stations. When normalized by the amount of used seismic data, the ergodicity was satisfied, which suggests that the minimum time-resolution of dv/v measurements is a function of the number of available stations. What is the highest time-resolution limit that one can reach? This question remains to be answered but our study demonstrates an important property of seismic interferometry from ambient noise correlations.

Thanks to the gained precision, we resolved a 0.4 per cent velocity drop after a seismic event that induced ∼1 cm s^{-1} of PGV at a 10-min resolution. Half of this drop was then recovered with a log-linear relaxation shape in agreement with slow dynamics studies. The largest changes were contained in the immediate aftermath of the earthquake. We showed that this relaxation behaviour is happening

in a hard rock site according to the local 1-D shear velocity profile we derived from the focal spot imaging technique and an McMC transdimensional Bayesian inversion.

ACKNOWLEDGMENTS

DATA AVAILABILITY

The data from the PESO network are available at the following doi: 10.14470/2S162326. Data from the PATCX station are accessible through the IPOC network (doi:10.14470/PK615318).

REFERENCES

Albaric, J., Kühn, D., Ohrnberger, M., Langet, N., Harris, D., Polom, U., Lecomte, I. & Hillers, G., 2021. Seismic monitoring of permafrost in Svalbard, Arctic Norway, *Seismol. Res. Lett.,* **92**(5), 2891–2904.

Bekele, A., Birgisson, B., Ryden, N. & Gudmarsson, A., 2017. Slow dynamic diagnosis of asphalt concrete specimen to determine level of damage caused by static low temperature conditioning, *AIP Conf. Proceed.,* **1806**, 1–7.

Bittner, J.A. & Popovics, J.S., 2021. Mechanistic diffusion model for slow dynamic behavior in materials, *J. Mech. Phys. Solids,* **150**, doi:10.1016/j.jmps.2021.104355.

Bodin, T., Sambridge, M., Tkalčić, H., Arroucau, P., Gallagher, K. & Rawlinson, N., 2012. Transdimensional inversion of receiver functions and surface wave dispersion, *J. geophys. Res,* **117**(2), 1–24.

Bonilla, L.F., Guéguen, P. & Ben-Zion, Y., 2019. Monitoring coseismic temporal changes of shallow material during strong ground motion with interferometry and autocorrelation, *Bull. seism. Soc. Am.,* **109**(1), 187–198.

Brantut, N., 2015. Time-dependent recovery of microcrack damage and seismic wave speeds in deformed limestone, *J. geophys. Res,* **120**(12), 8088–8109.

Brenguier, F., Campillo, M., Hadziioannou, C., Shapiro, N.M., Nadeau, R.M. & Larose, E., 2008. Postseismic relaxation along the San Andreas fault at Parkfield from continuous seismological observations., *Science (New York, N.Y.),* **321**(5895), 1478–81.

Budi-Santoso, A. & Lesage, P., 2016. Velocity variations associated with the large 2010 eruption of Merapi volcano, Java, retrieved from seismic multiplets and ambient noise cross-correlation, *Geophys. J. Int.,* **206**(1), 221–240.

Clements, T. & Denolle, M.A., 2018. Tracking groundwater levels using the ambient seismic field, *Geophys. Res. Lett.,* **45**(13), 6459–6465.

Conti, S., Roux, P. & Fink, M., 2002. Depth and range shifting of a focal spot using a time-reversal mirror in an acoustic waveguide, *Appl. Phys. Lett.,* **80**(19), 3647–3649.

Dietze, M., Cook, K.L., Illien, L., Rach, O., Puffpaff, S., Stodian, I. & Hovius, N., 2020. Impact of nested moisture cycles on coastal Chalk Cliff failure revealed by multiseasonal seismic and topographic surveys, *J. geophys. Res.,* **125**(8), doi:10.1029/2019JF005487.

Donaldson, C., Winder, T., Caudron, C. & White, R.S., 2019. Crustal seismic velocity responds to a magmatic intrusion and seasonal loading in Iceland's Northern Volcanic Zone, *Sci. Adv.,* **5**(11), doi:10.1126/sciadv.aax6642.

Dreiling, J. & Tilmann, F., 2019. BayHunter - McMC transdimensional Bayesian inversion of receiver functions and surface wave dispersion. V. 1.0. GFZ Data Services. https://doi.org/10.5880/GFZ.2.4.2019.001.

Dreiling, J., Tilmann, F., Yuan, X., Haberland, C. & Seneviratne, S.W., 2020. Crustal structure of Sri Lanka derived from joint inversion of surface wave

dispersion and receiver functions using a Bayesian approach, *J. geophys. Res,* **125**(5), 1–15.

Fichtner, A., Stehly, L., Ermert, L. & Boehm, C., 2017. Generalized interferometry - I: theory for interstation correlations, *Geophys. J. Int.,* **208**(2), 603–638.

Fink, M., 2008. Time-reversal acoustics, *J. Phys.: Conf. Ser.,* **118**(1), doi:10.1088/1742-6596/118/1/012001.

Gao, K., Rougier, E., Guyer, R.A., Lei, Z. & Johnson, P.A., 2019. Simulation of crack induced nonlinear elasticity using the combined finite-discrete element method, *Ultrasonics,* **98**, 51–61.

Gao, L., Shokouhi, P. & Rivière, J., 2022. Effect of relative humidity on the nonlinear elastic response of granular media, *J. appl. Phys.,* **131**(5), doi:10.1063/5.0073967.

Gassenmeier, M., Sens-Schönfelder, C., Delatre, M. & Korn, M., 2015. Monitoring of environmental influences on seismic velocity at the geological storage site for CO2 in Ketzin (Germany) with ambient seismic noise, *Geophys. J. Int.,* **200**(1), 524–533.

Gassenmeier, M., Sens-Schönfelder, C., Eulenfeld, T., Bartsch, M., Victor, P., Tilmann, F. & Korn, M., 2016. Field observations of seismic velocity changes caused by shaking-induced damage and healing due to mesoscopic nonlinearity, *Geophys. J. Int.,* **204**(3), 1490–1502.

GFZ German Research Centre For Geosciences, & Institut Des Sciences De L'Univers-Centre National De La Recherche CNRS-INSU, 2006. IPOC Seismic Network. Integrated Plate boundary Observatory Chile - IPOC. https://doi.org/10.14470/PK615318.

Groos, J.C. & Ritter, J. R.R., 2009. Time domain classification and quantification of seismic noise in an urban environment, *Geophys. J. Int.,* **179**(2), 1213–1231.

Guéguen, P., Bonilla, L.F. & Douglas, J., 2019. Comparison of soil nonlinearity (in situ stress-strain relation and G/G max reduction) observed in strong-motion databases and modeled in ground-motion prediction equations, *Bull. seism. Soc. Am.,* **109**(1), 178–186.

Guyer, R.A., Ten Cate, J. & Johnson, P., 1999. Hysteresis and the dynamic elasticity of consolidated granular materials, *Phys. Rev. Lett.,* **82**(16), 3280–3283.

Hadziioannou, C., Larose, E., Coutant, O., Roux, P. & Campillo, M., 2009. Stability of monitoring weak changes in multiply scattering media with ambient noise correlation: laboratory experiments, *J. acoust. Soc. Am.,* **125**(6), 3688–3695.

Hadziioannou, C., Larose, E., Baig, A., Roux, P. & Campillo, M., 2011. Improving temporal resolution in ambient noise monitoring of seismic wave speed, *J. geophys. Res,* **116**(7), 1–10.

Herrmann, R.B. & Ammon, C.J., 2002. Computer Programs in Seismology, Surface Waves, Receiver Functions and Crustal Structure, Version 3.30, St. Louis University, St. Louis, MO.

Hillers, G., Roux, P., Campillo, M. & Ben-Zion, Y., 2016. Focal spot imaging based on zero lag cross-correlation amplitude fields: application to dense array data at the San Jacinto fault zone, *J. geophys. Res,* **121**(11), 8048–8067.

Hobiger, M., Wegler, U., Shiomi, K. & Nakahara, H., 2014. Single-station cross-correlation analysis of ambient seismic noise: application to stations in the surroundings of the 2008 Iwate-Miyagi Nairiku earthquake, *Geophys. J. Int.,* **198**(1), 90–109.

Illien, L., Andermann, C., Sens-Schönfelder, C., Cook, K.L., Baidya, K.P., Adhikari, L.B. & Hovius, N., 2021. Subsurface moisture regulates Himalayan groundwater storage and discharge, *AGU Adv.,* **2**(2), doi:10.1029/2021av000398.

Illien, L., Sens-Schönfelder, C., Andermann, C., Marc, O., Cook, K.L., Adhikari, L.B. & Hovius, N., 2022. Seismic velocity recovery in the subsurface: transient damage and groundwater drainage following the 2015 Gorkha Earthquake, Nepal, *J. geophys. Res,* **127**(2), 1–18.

Knight, J.B., Fandrich, C.G., Ning Lau, C., Jaeger, H.M. & Nagel, S.R., 1995. Density relaxation in a vibrated granular material, *Phys. Rev. E,* **51**(5), doi:10.1103/PhysRevE.51.3957.

Kober, J., Gliozzi, A., Scalerandi, M. & Tortello, M., 2022. Material grain size determines relaxation-time distributions in slow-dynamics experiments, *Phys. Rev. Appl.,* **17**(1), doi:10.1103/PhysRevApplied.17.014002.

Lecocq, T., Longuevergne, L., Pedersen, H.A., Brenguier, F. & Stammler, K., 2017. Monitoring ground water storage at mesoscale using seismic noise: 30 years of continuous observation and thermo-elastic and hydrological modeling, *Sci. Rep.,* **7**(1), doi:10.1038/s41598-017-14468-9.

Lieou, C.K., Daub, E.G., Ecke, R.E. & Johnson, P.A., 2017. Slow dynamics and strength recovery in unconsolidated granular Earth materials: a mechanistic theory, *J. geophys. Res,* **122**(10), 7573–7583.

Lindner, F., Wassermann, J. & Igel, H., 2021. Seasonal freeze-thaw cycles and permafrost degradation on Mt. Zugspitze (German/Austrian Alps) revealed by single-station seismic monitoring, *Geophys. Res. Lett.,* **48**(18), 1–11.

Lobkis, O.I. & Weaver, R.L., 2001. On the emergence of the Green's function in the correlations of a diffuse field, *J. acoust. Soc. Am.,* **110**(6), 3011–3017.

Lu, Y. & Ben-Zion, Y., 2022. Regional seismic velocity changes following the 2019 Mw7.1 Ridgecrest, California earthquake from autocorrelations and P/S converted waves, *Geophys. J. Int.,* **228**(1), 620–630.

Manga, M., Beresnev, I., Brodsky, E.E., Elkhoury, J.E., Elsworth, D., Ingebritsen, S.E., Mays, D.C. & Wang, C.Y., 2012. Changes in permeability caused by transient stresses: field observations, experiments, and mechanisms, *Rev. Geophys.,* **50**(2), doi:10.1029/2011RG000382.

Marc, O., Hovius, N., Meunier, P., Uchida, T. & Hayashi, S., 2015. Transient changes of landslide rates after earthquakes, *Geology,* **43**(10), 883–886.

Marc, O., Sens-Schönfelder, C., Illien, L., Meunier, P., Hobiger, M., Sawazaki, K., Rault, C. & Hovius, N., 2021. Toward using seismic interferometry to quantify landscape mechanical variations after earthquakes, *Bull. seism. Soc. Am.,* **111**(3), 1631–1649.

Mavko, G., Mukerji, T. & Dvorkin, J., 2009. *The Rock Physics Handbook: Tools for Seismic Analysis of Porous Media,* 2nd edn, Cambridge Univ. Press.

McNicol, R., 1949. The fading of radio waves of medium and high frequencies, *Proc. IEEE - Part III: Radio Commun. Eng.,* **96**(44), 517–524.

Meyer, G.G., Brantut, N., Mitchell, T.M., Meredith, P.G. & Plümper, O., 2021. Time dependent mechanical crack closure as a potential rapid source of post-seismic wave speed recovery: insights from experiments in Carrara marble, *J. geophys. Res,* **126**(4), 1–29.

Moore, C.C., 2015. Ergodic theorem, ergodic theory, and statistical mechanics, *Proc. Natl. Acad. Sci. U. S. A.,* **112**(7), 1907–1911.

Mulargia, F. & Castellaro, S., 2013. A seismic passive imaging step beyond SPAC and ReMi, *Geophysics,* **78**(5), doi:10.1190/GEO2012-0405.1.

Nakamura, Y., 2000. Clear identification of fundamental idea of Nakamura's technique and its applications, in *Proceedings of the 12th World Conference on Earthquake Engineering,* Auckland, New Zealand, 30 January–4 February 2000, Paper no. 2656.

Nakata, N. & Snieder, R., 2012. Estimating near-surface shear wave velocities in Japan by applying seismic interferometry to KiK-net data, *J. geophys. Res,* **117**(1), doi:10.1029/2011JB008595.

Oakley, D.O., Forsythe, B., Gu, X., Nyblade, A.A. & Brantley, S.L., 2021. Seismic ambient noise analyses reveal changing temperature and water signals to 10s of meters depth in the critical zone, *J. geophys. Res.,* **126**(2), 1–21.

Oshima, M. & Takenaka, H., 2020. A P-and S-wave picking technique based on the probabilistic density function of seismic-waveform amplitude, *Bull. seism. Soc. Am.,* **110**(2), 763–782.

Ostrovsky, L., Lebedev, A., Riviere, J., Shokouhi, P., Wu, C., Stuber Geesey, M.A. & Johnson, P.A., 2019. Long-time relaxation induced by dynamic forcing in geomaterials, *J. geophys. Res.,* **124**(5), 5003–5013.

Overduin, P.P., Haberland, C., Ryberg, T., Kneier, F., Jacobi, T., Grigoriev, M.N. & Ohrnberger, M., 2015. Submarine permafrost depth from ambient seismic noise, *Geophys. Res. Lett.,* **42**(18), 7581–7588.

Qin, L., Ben-Zion, Y., Bonilla, L.F. & Steidl, J.H., 2020. Imaging and monitoring temporal changes of shallow seismic velocities at the Garner Valley Near Anza, California, following the M7.2 2010 El Mayor-Cucapah earthquake, *J. geophys. Res.,* **125**(1), 1–17.

Remillieux, M.C., Ulrich, T.J., Goodman, H.E. & Ten Cate, J.A., 2017. Propagation of a finite-amplitude elastic pulse in a bar of Berea sandstone:

a detailed look at the mechanisms of classical nonlinearity, hysteresis, and nonequilibrium dynamics, *J. geophys. Res.,* **122**(11), 8892–8909.

Richter, T., Sens-Schönfelder, C., Kind, R. & Asch, G., 2014. Comprehensive observation and modeling of earthquake and temperature-related seismic velocity changes in northern Chile with passive image interferometry, *J. geophys. Res.,* **119**(6), 4747–4765.

Rivet, B., Girin, L. & Jutten, C., 2007. Log-Rayleigh distribution: a simple and efficient statistical representation of log-spectral coefficients, *IEEE Trans. Audio, Speech Lang. Process.,* **15**(3), 796–802.

Rost, S. & Thomas, C., 2002. Array seismology: methods and applications, *Rev. Geophys.,* **40**(3), 2–1-2-27.

Sawazaki, K., Saito, T. & Shiomi, K., 2018. Shallow temporal changes in S wave velocity and polarization anisotropy associated with the 2016 Kumamoto earthquake sequence, Japan, *J. geophys. Res.,* **123**(11), 9899–9913.

Sens-Schönfelder, C. & Brenguier, F., 2019. Noise-based monitoring, in *Seismic Ambient Noise,* Chapter 9, pp. 267–301, eds Nakata, N., Gualtieri, L. & Fichtner, A., Cambridge Univ. Press.

Sens-Schönfelder, C. & Eulenfeld, T., 2019. Probing the in situ elastic nonlinearity of rocks with Earth tides and seismic noise, *Phys. Rev. Lett.,* **122**(13), doi:10.1103/PhysRevLett.122.138501.

Sens-Schönfelder, C. & Wegler, U., 2006. Passive image interferometry and seasonal variations of seismic velocities at Merapi Volcano, Indonesia, *Geophys. Res. Lett.,* **33**(21), doi:10.1029/2006GL027797.

Sens-Schönfelder, C., Pomponi, E. & Peltier, A., 2014. Dynamics of Piton de la Fournaise volcano observed by passive image interferometry with multiple references, *J. Volc. Geotherm. Res.,* **276**, 32–45.

Sens-Schönfelder, C., Snieder, R. & Li, X., 2019. A model for nonlinear elasticity in rocks based on friction of internal interfaces and contact aging, *Geophys. J. Int.,* **216**(1), 319–331.

Sheng, Y., Ellsworth, W.L., Lellouch, A. & Beroza, G.C., 2021. Depth constraints on coseismic velocity changes from frequency-dependent measurements of repeating earthquake waveforms, *J. geophys. Res.,* **126**(2), 1–12.

Shokouhi, P., Rivière, J., Guyer, R.A. & Johnson, P.A., 2017. Slow dynamics of consolidated granular systems: multi-scale relaxation, *Appl. Phys. Lett.ers,* **111**(25), doi:10.1063/1.5010043.

Shokouhi, P., Jin, J., Wood, C., Rivière, J., Madara, B., Elsworth, D. & Marone, C., 2020. Dynamic stressing of naturally fractured rocks: on the relation between transient changes in permeability and elastic wave velocity, *Geophys. Res. Lett.,* **47**(1), 1–10.

Sleep, N.H. & Nakata, N., 2017. Nonlinear attenuation of S waves by frictional failure at shallow depths, *Bull. seism. Soc. Am.,* **107**(4), 1828–1848.

Snieder, R., Sens-Schönfelder, C. & Wu, R., 2016. The time dependence of rock healing as a universal relaxation process, a tutorial, *Geophys. J. Int.,* **208**(1), 1–9.

Takano, T., Nishimura, T., Nakahara, H., Ohta, Y. & Tanaka, S., 2014. Seismic velocity changes caused by the Earth tide: ambient noise correlation analyses of small-array data, *Geophys. Res. Lett.,* **41**(17), 6131–6136.

Tapia, J., González, R., Townley, B., Oliveros, V., Álvarez, F., Aguilar, G., Menzies, A. & Calderón, M., 2018. Geology and geochemistry of the Atacama Desert, Antonie van Leeuwenhoek, *Int. J. Gen. Mol. Microbiol.,* **111**(8), 1273–1291.

TenCate, J.A., Smith, E. & Guyer, R.A., 2000. Universal slow dynamics in granular solids, *Phys. Rev. Lett.,* **85**(5), 1020–1023.

Viens, L. & Van Houtte, C., 2020. Denoising ambient seismic field correlation functions with convolutional autoencoders, *Geophys. J. Int.,* **220**(3), 1521–1535.

Viens, L., Denolle, M.A., Hirata, N. & Nakagawa, S., 2018. Complex near-surface rheology inferred from the response of greater Tokyo to strong ground motions, *J. geophys. Res.,* **123**(7), 5710–5729.

Xu, Y., Lebedev, S., Meier, T., Bonadio, R. & Bean, C.J., 2021. Optimized workflows for high-frequency seismic interferometry using dense arrays, *Geophys. J. Int.,* **227**(2), 875–897.

Yoritomo, J.Y. & Weaver, R.L., 2020. Slow dynamics in a single glass bead, *Phys. Rev. E,* **101**(1), 1–14.

SUPPORTING INFORMATION

Supplementary data are available at *GJI* online.

Figure S1. Screenshot of the array in Google Earth. The yellow pins stand for the PESO stations. The picture highlights the cliff escarpment. The shoreline orientation is in agreement with the beamforming results in which the noise strikes the array from a south-west direction.

Figure S2. Proportion of daily muted segments. Each colour stands for a different station.

Figure S3. Illustration of the similarity matrix. On the left, we report the similarity matrix when using only one autocorrelation at one station. The blue dots show the stretching value corresponding to the best correlation values in the eq. (4) of the main text. On the right, we show the similarity matrix built when stacking all the possible matrices (such as the one on the left) of the network. The figure illustrates the enhancement of the measure using this technique.

Figure S4. Beamforming results (at 3–6 Hz) for the 22nd of October 2018. Each azimuthal plot indicates beamforming results for 3-hr-long slices. Corresponding times are indicated above each plot. In the afternoon, note the slight perturbation of the noise wavefield from the NE direction.

Figure S5. Average envelope of the horizontal components in the network during coseismic ground shaking. The time 0 corresponds to the onset of the *P* wave. The envelope is averaged over all the network.

Figure S6. Inversion results when adding the observation from the beamforming method. (a) Inferred shear velocity profile interpolated at a 50 m resolution. Green and blue lines shows the mean and the median value of the best retained models. Dashed black lines indicated the standard deviation. (b) Histogram of the depth of the inferred layer structures (c) The green line shows the dispersion curve that we use for the inversion, the other curves showing the best fit obtained for each chains. Histograms corresponding to the other inverted parameters are shown in (d) for the number of layers, in (e) for the noise level in the measurements and in (f) for the Vp/Vs ratio.

Figure S7. Geological media observed in the field. The geology hints at clasts embedded in a matrix containing large amounts of evapourites (likely gypsum and halite). The picture is taken from the study of Sens-Schönfelder & Eulenfeld (2019).

Figure S8. Rayleigh wave sensitivity given the inferred 1-D profile and the measured dispersion curve. The kernel was computed using the CPS software (Herrmann & Ammon 2002).

Please note: Oxford University Press is not responsible for the content or functionality of any supporting materials supplied by the authors. Any queries (other than missing material) should be directed to the corresponding author for the paper.